Nonlinear Dyn (2025) 113:9605–9623
https://doi.org/10.1007/s11071-024-10614-x

RESEARCH

Structural nonlinear boundary condition identification using a hybrid physics data-driven approach

Lanxin Luo · Limin Sun · Yixian Li · Yong Xia

Received: 21 June 2024 / Accepted: 5 November 2024 / Published online: 23 November 2024

Abstract As civil infrastructures often exhibit nonlinearities, the identification of nonlinear behaviors is crucial to assess the structural safety state. However, existing physics-driven methods can only estimate the nonlinear parameters given a known nonlinear behavior pattern. By contrast, the data-driven methods can merely map the load-response relationship at the structural level, rather than identify an accurate nonlinear mapping relationship at the component level. To address these issues, a hybrid physics-data-driven strategy is developed in this study to identify the blind nonlinearity. The nonlinear structural components are surrogated by a data-driven multilayer perceptron, and the linear ones are simulated by using the finite element method. Subsequently, the global stiffness matrix and restoring force vector are assembled according to the elemental topology relationship to obtain the hybrid model. The discrepancy between the measured and hybrid model-predicted responses is formulated as the loss function, by minimizing which of the MLPs are indirectly trained and the nonlinearities can be identified without knowing the nonlinearity type. Three numerical cases are used to verify the proposed method in identifying the elastic, hysteretic, and multiple nonlinear boundary conditions. Results show that the proposed method is robust given different noise levels, sensor placements, and nonlinear types. Moreover, the trained hybrid model possesses a strong generalization ability to accurately predict full-field structural responses.

Keywords Nonlinear boundary condition · Blind nonlinearity identification · Finite element method · Physics-informed neural network · Stabilized central difference method

Limin Sun: co-first author.

L. Luo · L. Sun
Department of Bridge Engineering, Tongji University, Shanghai, China

L. Luo · Y. Li (✉) · Y. Xia (✉)
Department of Civil and Environmental Engineering, The Hong Kong Polytechnic University, Hong Kong, China
e-mail: yixian.li@polyu.edu.hk

Y. Xia
e-mail: ceyxia@polyu.edu.hk

L. Luo · Y. Li · Y. Xia
Joint Research Centre for Marine Infrastructure, The Hong Kong Polytechnic University, Hong Kong, China

L. Sun
State Key Laboratory of Disaster Reduction in Civil Engineering, Tongji University, Shanghai, China

L. Sun
Shanghai Qizhi Institute, Shanghai, China

1 Introduction

Nonlinear phenomena are unambiguously observed in engineering structures during their operation, and nonlinearity modeling and analysis are thus important for structural response prediction, damage identification, and conditions assessment [1, 2]. The structural nonlinear behavior can be categorized into material [3], boundary [4], and geometric [5] nonlinearities. In civil engineering, nonlinear boundary conditions are common and related to the safety and stability of infrastructures. The bridge bearings can be disrupted due to material deterioration [6] and obstruction [7], leading to nonlinear contact and frictional forces. The seismic and wind-resistant bearings [8] are designed with hysteretic nonlinearity for vibration mitigation. They dissipate energy from seismic and wind loads, thus reducing the risk of structural damage. In the realm of vibration control, the rubber dampers at the ends of stay cables [9] and dampers between the building floors [10] also exhibit nonlinear behaviors. Additionally, the nonlinear constitutive behavior of soil and the nonlinear interaction between piles and soil make nonlinear boundary conditions particularly common in foundation and geotechnical engineering [11]. The boundary region is also usually enclosed and confined in spaces, resulting in the direct evaluation of the boundaries being challenging [12]. The indirectly nonlinear boundary identification therefore becomes an effective approach to address these issues.

The nonlinear systems identification methods can be categorized into physics- and data-driven approaches [2]. In structural engineering, the structural parameters are identified based on unbiased filters and finite element model (FEM) updating. In the filter-based methods, the system identification problem is transformed as a state estimation problem, where the unknown structural parameters are regarded as state variables, such as the extended Kalman filter (EKF) [13], unscented Kalman filter (UKF) [14], and cubature Kalman filter (CKF) [15]. The analytical linearization in EKF could lead to divergence [16]. Lei et al. developed extended Kalman filters with unknown input (EKF-UI) [17] and unscented Kalman filters with unknown input (UKF-UI) [18, 19] to jointly identify the input and state of systems with nonlinear linking components (e.g., springs, dampers). In FEMU-based approaches, the under-determined parameters are identified via optimization techniques. Tian et al. [20, 21] employed the substructuring method to calculate the response sensitivity and identify systems with nonlinear linking components. Song et al. proposed a nonlinear normal modes-based model updating method to handle the geometric nonlinearity in a numerical cantilever beam [22] and boundary nonlinearity in a wing-engine structure [23]. The physics-driven methods require comprehensive prior knowledge of the nonlinear behaviors [2] by assuming the constitutive model as a given nonlinear model, which is impractical. Some researchers have therefore endeavored to approximate nonlinear constitutive models using polynomial functions [24] but with limited accuracy [25].

Deep learning technology can well address the prior-dependent issue of conventional physics-driven methods. Due to their strong nonlinear fitting capability, neural networks (NNs) are able to learn structural nonlinear behaviors from abundant training data, thus eliminating the need for prior physical knowledge [26]. The convolutional neural network (CNN) [27] and long short-term memory (LSTM) network [28] were used to predict the dynamic response of nonlinear structures in a purely data-driven manner. However, purely data-driven methods are black-box models lacking physical interpretability, where the behaviors of the trained NNs cannot be well understood and controlled [29].

In recent years, physics-informed neural networks (PINNs) have been developed to address the mentioned issues of pure data-driven methods by integrating physics knowledge into the neural network models. PINN can reduce training data requirements and enhance the robustness, interpretability, and generalization of the trained NN models [29–31]. PINNs are adopted for nonlinear system identification, and they can be broadly categorized as weak and

strong constraint methods. In weak constraint PINN, the physical laws are formulated as the loss function as a weak regularization term. Zhang et al. integrated physical laws, including the equation of motion, state dependency, and hysteretic constitutive relationships, into CNN [32] and LSTM networks [33] for metamodeling structural systems with nonlinear dampers. Liu et al. [34] proposed a PINN combining data loss and physics loss based on state dependency and rate-dependent behavior for multi-physics nonlinear structural system identification. Zhai et al. [35] proposed a PINN adopting the framework of the fourth-order Runge–Kutta method and incorporating the physics loss based on automatic differentiation function for dynamical system parameter estimation and modeling. Yamaguchi et al. [36] incorporated the data loss and physics loss derived from the Newmark-beta method into a PINN for the nonlinear boundary and damage identification of a reinforced concrete bridge pier. It should be noted that the physical loss weight is an essential hyperparameter in these methods and should be carefully selected to avoid misdirecting the training process. In the second kind of PINN, the physics knowledge is embedded as strong constraints to form the architecture of the entire model, where the physics relationships are strictly obeyed. Eshkevari et al. developed a recursive neural network based on the Newmark-beta and Newton–Raphson methods framework to metamodel the nonlinear system and estimate the full-field structural dynamic response [37]. Bacsa et al. proposed a variational autoencoder that incorporates Hamiltonian NNs to enforce symplectic constraints on the inferred posterior distribution for learning dynamics of systems with nonlinear springs [38]. Liu et al. introduced a probabilistic physics-guided framework that connects state-space models with deep Markov models, allowing for the unsupervised learning and identification of nonlinear dynamical systems [39]. Liu et al. recently utilized neural networks to parameterize the modeling of process dynamics and sensory observations in EKF, enabling form-free learning and prediction of nonlinear structural dynamics [40]. However, these data-driven studies solely focus on the mapping relationship at the structure level, such as global load-response pairs, and they overlooked the mechanical behavior at the component level, such as elemental response-internal force pairs of the boundary. Therefore, they cannot identify the nonlinear boundary conditions.

In material nonlinearity identification, the NNs have been employed to replace material constitutive functions in FEMs [41–43], providing a novel perspective for nonlinear model identification. Ghaboussi et al. first adopted NNs to learn the material nonlinear constitutive models with paired strain–stress datasets collected from static experiments [44]. They further developed autoprogressive models [45] and self-learning FE models [46] to expand the data type available by converting static load–deflection experimental data into strain–stress data through a two-step FE simulation. Huang et al. integrated the NN into a nonlinear Poisson equation and utilized the residual of the governing function as the loss function to indirectly train the NN model, eliminating the laborious collection of the paired strain–stress data [47]. However, this method requires full-field displacement measurements. To facilitate the learning from limited observation data, Liu et al. [48] and Xu et al. [49] further employed the discrepancy between incomplete measurements and predictions as the training loss. In these studies, the nonlinear capabilities of NNs were well integrated with the physical knowledge from FE models, enabling the identification of material constitutive models from the measured responses. However, these studies are confined to static structural analysis, and they are impractical because the static response data are challenging to collect for the operational infrastructures.

To address these issues, an FEM-NN hybrid approach combined with a stabilized central difference (SCD) solver is developed in this study to identify the nonlinear boundary conditions from dynamic measurements. The complex nonlinear boundary behaviors are modeled by NNs, while the

linear structural components are simulated with FE methods. They are then assembled to form the hybrid model according to the elemental topology. Finally, the discrepancy between measured and hybrid model-predicted responses is formulated as the loss function to indirectly train the NNs. The highlights of the proposed method include the following aspects:

(1) A physics-data co-driven hybrid approach is developed for blind nonlinearity identification with unknown nonlinearity type and parameters.
(2) The hybrid model is trained in a novel unsupervised manner, where the structural response data instead of a nonlinear behavior dataset are needed to identify the nonlinearity.
(3) The developed method possesses high applicability and generalization in identifying the elastic, hysteretic, and multiple nonlinear boundaries for multiple degree-of-freedom systems.

The remaining paper is organized as follows: the basic techniques used in the hybrid modeling are introduced in Sect. 2, followed by the nonlinear boundary condition identification strategy in Sect. 3. Three cases are investigated in Sects. 4, 5 and 6 to verify the accuracy and robustness of the proposed method in identifying elastic, hysteretic, and multiple nonlinear boundary conditions. The associated conclusions are drawn in Sect. 7.

2 Preliminaries

2.1 Stabilized central difference method

The governing equation for a nonlinear dynamic system is expressed as follows to describe the relationships between the structural property, states, and external forces:

$$\boldsymbol{Ma} + \boldsymbol{Cv} + \boldsymbol{F}^{\boldsymbol{r}}(\boldsymbol{u}, \boldsymbol{v}) = \boldsymbol{P} \tag{1}$$

where $\boldsymbol{M}$ and $\boldsymbol{C}$ represent the global mass, and damping matrixes, respectively; $\boldsymbol{u}$, $\boldsymbol{v}$, and $\boldsymbol{a}$ denote nodal displacement, velocity, and acceleration vectors, respectively. The restoring force $\boldsymbol{F}^{\boldsymbol{r}}(\boldsymbol{u}, \boldsymbol{v})$ is associated with the structural state variables. For elastic linear systems, $\boldsymbol{F}^{\boldsymbol{r}}(\boldsymbol{u}, \boldsymbol{v}) = \boldsymbol{Ku}$, where $\boldsymbol{K}$ is the stiffness matrix. $\boldsymbol{P}$ represents the load vector.

The time domain methods are commonly used in nonlinear analysis to solve Eq. (1), and they can be classified into explicit and implicit methods. The implicit methods, such as Newmark-beta [50] and Runge–Kutta [51] methods, employ iterations in each time step to approximate the structural state of the subsequent time step, where the Newton–Raphson algorithm is often adopted. In addition, they face the problems of excessive computational burden and potential divergence. By contrast, explicit methods, such as the central difference method [52], use the state variables at the current step to derive those at the next time step without iterations. However, the explicit methods are conditionally stable, and the time step should thus be carefully selected according to the natural frequency of the analyzed structure.

To balance the computational cost and stability, the SCD method [53] is adopted to calculate the structural responses with nonlinear boundaries. SCD is an explicit method as detailed in Algorithm 1. The selective mass scaling technique is adopted to add artificial masses to the origin structure, thereby reducing high-frequency responses that constitute a minor portion of the overall response but are prone to divergence. Meanwhile, it does not affect low-frequency accuracy significantly [54].

In the algorithm, $\boldsymbol{M}$, $\boldsymbol{C}$, and $\boldsymbol{K}$ denote the mass, damping, and stiffness matrixes of the known linear part of the structure, respectively. $\boldsymbol{K}^{\boldsymbol{T}}$ represents the structural tangent stiffness matrix, and $\widehat{\boldsymbol{M}}$ represents the revised mass matrix. $\boldsymbol{K}^{\boldsymbol{s}}$, $\boldsymbol{F}^{\boldsymbol{s}}$ represent the stiffness matrix and restoring force vector due to the nonlinear boundaries. Specifically, $\boldsymbol{K}^{\boldsymbol{s}}$ is a diagonal matrix defined by $\boldsymbol{K}^{\boldsymbol{s}}(\boldsymbol{r}, \boldsymbol{r}) = \boldsymbol{k}_{\boldsymbol{r}}^{\boldsymbol{s}}$, where r denotes the DOF numbers of the nonlinear boundaries. $\boldsymbol{k}_{\boldsymbol{r}}^{\boldsymbol{s}}$ represents the stiffness of the nonlinear component associated with the rth DOF. $\boldsymbol{F}^{\boldsymbol{s}}(\boldsymbol{r}) = \boldsymbol{f}_{\boldsymbol{r}}^{\boldsymbol{s}}$, with all other elements being zero. Here, $\boldsymbol{f}_{\boldsymbol{r}}^{\boldsymbol{s}}$ denotes the restoring force of the nonlinear component at the rth DOF. In this study, the restoring force is nonlinear and dependent on displacement time history. For the nonlinear component at the rth DOF, $\boldsymbol{k}_{\boldsymbol{ir}}^{\boldsymbol{s}}$ at the ith time step is defined as the partial derivative of $\boldsymbol{f}_{\boldsymbol{ir}}^{\boldsymbol{s}}$ to the displacement $\boldsymbol{u}_{\boldsymbol{ir}}^{\boldsymbol{s}}$, i.e., $\boldsymbol{k}_{\boldsymbol{ir}}^{\boldsymbol{s}} = \frac{\partial f_{ir}^{s}}{\partial u_{ir}^{s}}$. $\boldsymbol{dt}$ is the time step length, and $\boldsymbol{\omega}_{\boldsymbol{i}}^{\boldsymbol{m}}$ represents the maximal structural frequency at the ith step. The structure is assumed to be initially in the equilibrium position, that is, the initial structural state vector composed of displacement and velocity is zero.

Algorithm 1. SCD method for nonlinear dynamic response calculation.

(1) Calculation for the initial time step

$\boldsymbol{F}_0^r = \boldsymbol{K}\boldsymbol{u}_0 + \boldsymbol{F}^s(\boldsymbol{x}_0), \boldsymbol{K}_0^T = \boldsymbol{K} + \boldsymbol{K}^s(\boldsymbol{x}_0)$

$\widehat{\boldsymbol{M}}_0 = \left(\boldsymbol{M} + dt\boldsymbol{C} + \alpha_0 \boldsymbol{K}^T dt^2\right), \alpha_0 = \frac{1}{4}\tanh\left(\frac{1}{4}\omega_0^m dt\right)$

$\boldsymbol{a}_0 = \widehat{\boldsymbol{M}}_0^{-1}\left(\boldsymbol{P}_0 - \boldsymbol{C}\boldsymbol{v}_0 - \boldsymbol{F}_0^r\right)$

$\boldsymbol{u}_{-1} = \boldsymbol{u}_0 - \boldsymbol{v}_0 dt + \frac{(dt)^2}{2}\boldsymbol{a}_0$

(2) Calculation for each time step

for i=0 to N_i-1, do

$\boldsymbol{F}_i^r = \boldsymbol{K}\boldsymbol{u}_i + \boldsymbol{F}^s(\boldsymbol{x}_i), \boldsymbol{K}_i^T = \boldsymbol{K} + \boldsymbol{K}^s(\boldsymbol{x}_i)$

$\widehat{\boldsymbol{M}}_i = \left(\boldsymbol{M} + \frac{1}{2}dt\boldsymbol{C} + \alpha_i \boldsymbol{K}^T dt^2\right), \alpha_i = \frac{1}{4}\tanh\left(\frac{1}{4}\omega_i^m dt\right)$

$\boldsymbol{u}_{i+1} = 2\boldsymbol{u}_i - \boldsymbol{u}_{i-1} + \left(\widehat{\boldsymbol{M}}_i + \frac{1}{2}dt\boldsymbol{C}\right)^{-1}\left[dt^2\left(\boldsymbol{P}_i - \boldsymbol{F}_i^r\right) - dt\boldsymbol{C}(\boldsymbol{u}_i - \boldsymbol{u}_{i-1})\right]$

$\boldsymbol{v}_i = \frac{\boldsymbol{u}_{i+1} - \boldsymbol{u}_{i-1}}{2dt}$

$\boldsymbol{a}_i = \frac{\boldsymbol{u}_{i+1} - 2\boldsymbol{u}_i + \boldsymbol{u}_i}{(dt)^2}$

end for

$\boldsymbol{u}, \boldsymbol{v}, \boldsymbol{a} = (\boldsymbol{u}_0, \ldots, \boldsymbol{u}_{N_i-1}), (\boldsymbol{v}_0, \ldots, \boldsymbol{v}_{N_i-1}), (\boldsymbol{a}_0, \ldots, \boldsymbol{a}_{N_i-1})$

Return: $\boldsymbol{u}, \boldsymbol{v}, \boldsymbol{a}$

2.2 Multilayer perceptron

The multilayer perceptron (MLP) is the foundation for numerous modern artificial intelligence applications, and it is still widely used nowadays [55]. In structural engineering, MLPs are adopted for bridge influence surface identification [56], damage detection [57, 58], structural condition assessment [59], nonlinear function fitting [60, 61], etc. MLP is a feedforward NN comprised of multiple layers (Fig. 1a). Each layer in an MLP includes multiple neurons connected to the adjacent layers through weights, bias, and activation functions, as detailed in Fig. 1b [62]. The nonlinear activation functions enable the MLP to effectively learn and model nonlinear behaviors, while the high-dimensional weights and biases allow the MLP to accurately fit complex models and datasets. Therefore, MLP is used to identify the boundary nonlinearities in this study. Each training epoch of an MLP starts from calculating the loss function by measuring the discrepancy between the real and predicted structural responses. Next, the partial derivatives of the loss function to each weight and bias parameters are computed. These derivatives inform the necessary adjustments for these parameters, which are then propagated and updated using the backpropagation algorithm to minimize the loss function iteratively. The details of MLP can also be referred to [63].

Given that the boundary condition is highly nonlinear in practice, representing the restoring force of

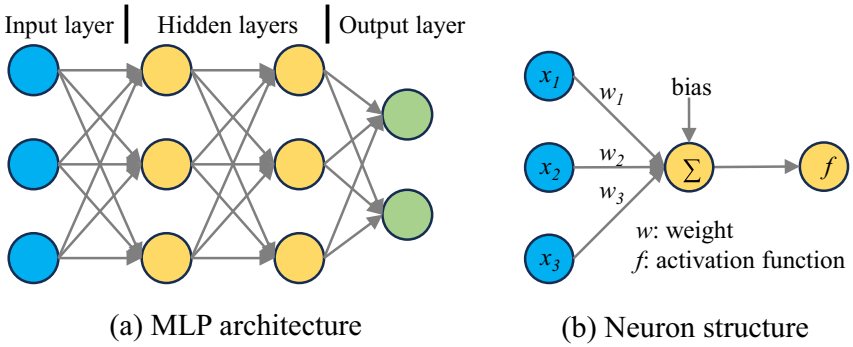

(a) MLP architecture (b) Neuron structure

Fig. 1 Schematic diagram of the multilayer perceptron

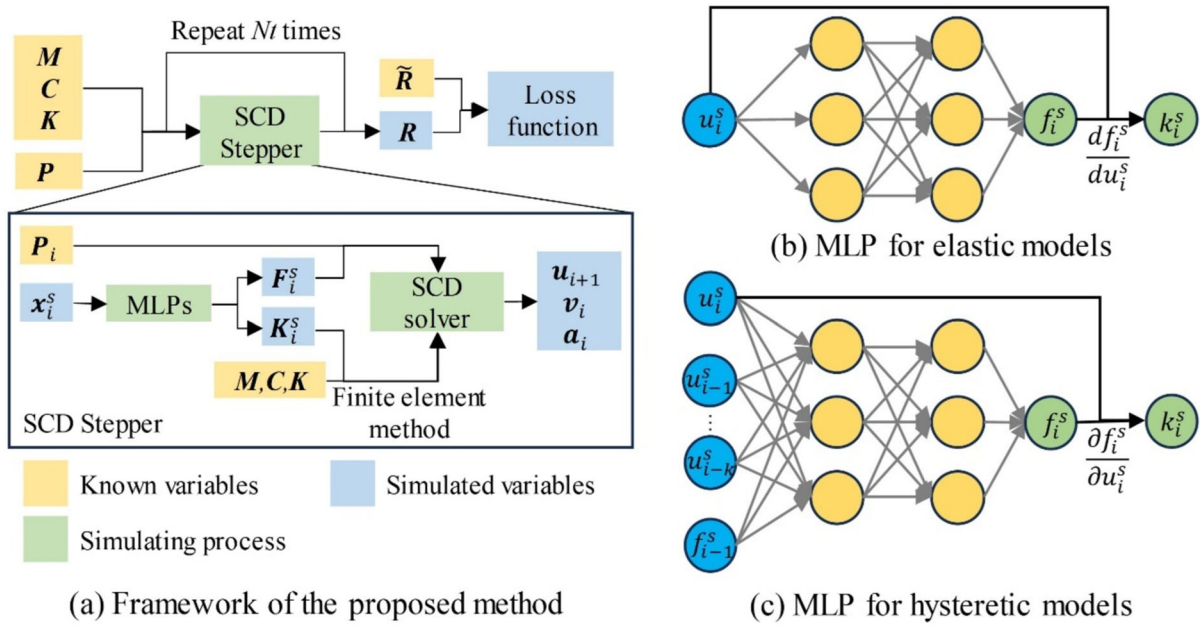

Fig. 2 Framework of the FEM-NN hybrid model with MLPs for nonlinear boundary condition identification

the nonlinear component using an MLP is appropriate. The displacement vector is the MLP input, and the restoring force of the nonlinear component is the output. The stiffness of the nonlinear component is calculated using the partial derivatives of the MLP output to the input through automatic differentiation. The MLP can be implemented on the PyTorch platform [64], which facilitates the symbolic definition of partial derivatives. The gradient in the MLP is calculated by using the automatic differentiation method [65].

3 Physics-data-driven nonlinearity identification

3.1 General framework

The proposed physics-data-co-driven nonlinearity identification method is summarized in Fig. 2a. The mass $\boldsymbol{M}$, damping $\boldsymbol{C}$, and stiffness $\boldsymbol{K}$ matrices of the linear structural components are calculated based on the FEM. The SCD stepper refers to steps 2 to 6 in the time iteration of Algorithm 1. In the SCD stepper, the unknown nonlinear boundary is simulated by an MLP. The input of the MLP is the state variable $\boldsymbol{x}$, and the output is the restoring force $\boldsymbol{f^s}$. The stiffness matrix associated with the nonlinear boundary, $\boldsymbol{k^s}$, is modeled using the partial derivatives of the MLP output to the boundary displacement at the current step $\boldsymbol{u_i}$ through automatic differentiation, i.e., $\boldsymbol{f^s(x) = MLP(x)}$, $\boldsymbol{k^s(x) = \frac{\partial MLP(x)}{\partial u_i}}$. Subsequently, the FE model-generated K and MLP-generated $\boldsymbol{K^s(x)}$ are assembled as the global stiffness matrices $\boldsymbol{K^T}$. The full-field responses R of this hybrid system are calculated by using the SCD method. In each epoch, the predicted responses R and measured responses $\widetilde{\boldsymbol{R}}$ are used to establish the loss function, by minimizing which the MLPs in the framework are indirectly trained. In such a way, the MLP is embedded in the calculation of the nonlinear structural responses, and it can be indirectly trained by minimizing the response loss. The MLPs can therefore approach the real nonlinear boundary condition by minimizing the loss function.

3.2 Nonlinearity surrogate model

The MLPs are adopted to approximate the nonlinear boundary conditions, where the stiffness and restoring force of the nonlinear components are estimated from the observed structural responses. The MLP architectures for the elastic and hysteretic boundary conditions

are depicted in Figs. 2b and c, respectively. The inputs of these two MLPs are different because the restoring force of an elastic component depends only on the current displacement, while that of a hysteretic component relates to the displacement history. Therefore, the displacement at the previous k time steps is considered in the hysteretic model in Fig. 2c. Since the time-dependent property of the nonlinear hysteretic model is unknown in advance, it is essential to choose a proper k to ensure both calculation efficiency and identification accuracy. A relatively small initial value of k, such as 2, can be first employed, and k is increased one by one in subsequent training until the loss function is reduced to a satisfactory level. The stiffness of the nonlinear component is calculated as the partial derivative of the outputted restoring force to the current displacement, for which the automatic differentiation tool in PyTorch is used.

3.3 Loss function

The variance-normalized mean square error (NMSE) loss function is used to train the data-driven model in the hybrid framework. The loss function L in this study is defined as the averaged NMSE between the reconstructed and measured responses:

$$L = \frac{1}{N_m}\sum_{m=1}^{N_m}\frac{\sum_{i=1}^{N_i}\left(\boldsymbol{R}_{m,i} - \widetilde{\boldsymbol{R}}_{m,i}\right)^2}{\mathrm{Var}\left(\widetilde{\boldsymbol{R}}_m\right)} \tag{2}$$

where N_m represents the total number of measurements, and m denotes the measurement index. N_i represents the total number of time steps, and i denotes the time step, and. Var is the variance of a vector. $\boldsymbol{R}$ and $\widetilde{\boldsymbol{R}} \in \mathbb{R}^{N_m \times N_i}$ are reconstructed and measured response matrixes.

4 Case I: A three-DOF spring-mass system with an elastic nonlinear spring

In this section, a nonlinear spring-mass system with three DOFs, as depicted in Fig. 3, is used to verify the proposed method. The three masses are $m_1 = m_2 = m_3 = 1 \times 10^6$ kg, and they are connected by two linear springs. m_1 and the ground are connected by a linear spring and an elastic nonlinear spring. The stiffness parameters of the three linear springs are $k_1 = k_2 = k_3 = 4 \times 10^5$ kN/m. The natural frequencies of the spring-mass system are 1.417, 3.969, and 5.736 Hz. The restoring force-response curves of the three types of elastic nonlinear springs, namely, softening, hardening, and anisotropic, are presented in Figs. 4a–c, respectively. The primary case utilizes the softening spring for illustration, while the hardening and anisotropic springs will be employed for comparative analysis. The restoring force-response curve of the elastic softening nonlinear spring is shown in Fig. 4a. The elastic softening boundary condition is frequently observed in vibration isolators. The overall softening characteristic with quasi-zero stiffness behavior far from the static equilibrium point can enhance the low-frequency vibration isolation performance [66]. Rayleigh damping is assumed for the whole structure, and the first two damping ratios are both 2%. The white noise load is applied to m_3 to excite the dynamic responses. In this case, three accelerometers are installed at a sampling frequency of 100 Hz, corresponding to 0.01 s time step in FE analysis. The acceleration and input force measurements are used to identify the nonlinear model.

The Pearson correlation coefficient (R) and the mean relative error (MRE) are used to measure the shape correlation and deviation of predictions and measurements:

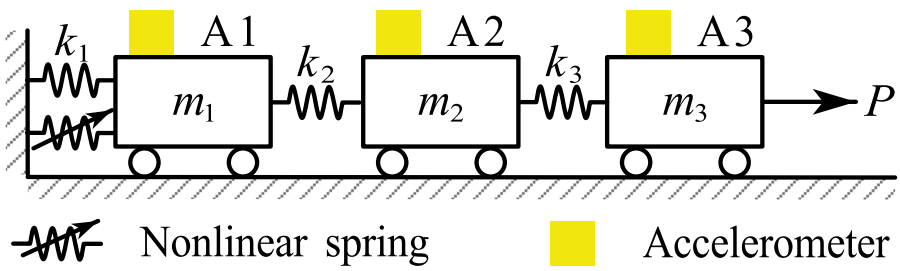

Fig. 3 Three-DOF spring-mass system with a nonlinear spring

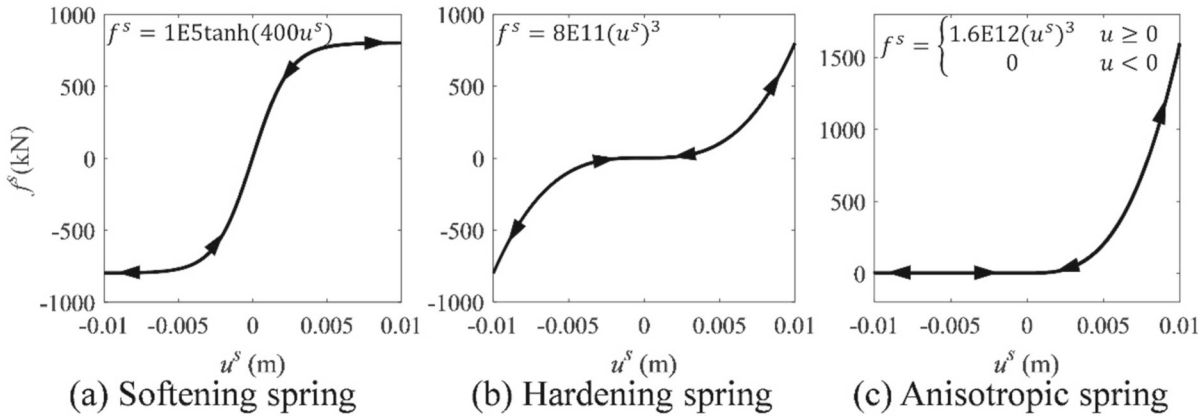

Fig. 4 Three elastic nonlinear springs utilized in Case I

Table 1 Architecture of the MLP

Layer number	Layer type	Size	Activation function
1	Input	n (input number)	–
2	Linear	500	Tanh
3	Linear	500	Tanh
4	Linear	500	Tanh
5	Linear	500	Tanh
6	Output	1	–

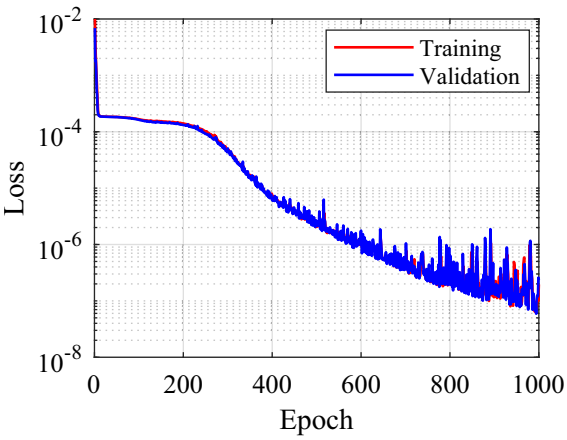

Fig. 5 Training and validation losses

$$\mathrm{R} = \frac{\mathrm{Cov}(\boldsymbol{r}, \widetilde{\boldsymbol{r}})}{\sqrt{\mathrm{Var}(\boldsymbol{r}) \bullet \mathrm{Var}(\widetilde{\boldsymbol{r}})}} \tag{3}$$

$$\mathrm{MRE} = \frac{\mathrm{Avg}(|\boldsymbol{r} - \widetilde{\boldsymbol{r}}|)}{\mathrm{Max}(|\widetilde{\boldsymbol{r}}|)} \tag{4}$$

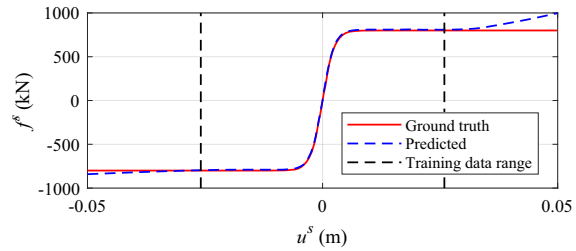

Fig. 6 Learned nonlinear boundary conditions using measurement without noise

where $\boldsymbol{r}$ and $\widetilde{\boldsymbol{r}}$ are prediction and ground truth vectors, respectively. They can represent the structural responses or boundary conditions. Cov(•) represents the covariance of two vectors, Avg(•) represents the mean value, and Max(•) represents the maximum. In practice, the two vectors are regarded as highly correlated when $R > 0.8$, and the prediction accuracy is considered acceptable when MRE $< 5\%$.

4.1 Network training

An MLP with four hidden layers is used to simulate the nonlinear spring (Table 1). In Case I, the spring is elastic and the input number n is thereby set as 1. The hybrid model and algorithm are implemented on the PyTorch platform. A total of 1,024 numerical samples are collected in the training dataset. Each sample segment is 512 long, namely, its duration is 5.12 s (512 × 0.01 s). The training–validation ratio is 8:2. The hybrid model is trained using the Adam optimizer with a batch size of 128 and a learning rate of 1×10^{-3}. The computer configuration includes an

Table 2 R and MRE between learned and true boundary conditions in all cases

Scenarios				R	MRE (%)
Case I	Noise level (%)	N0	0	0.999	1.449
		N1	5	0.999	1.518
		N2	10	0.999	1.846
		N3	20	0.999	1.963
		N4	30	0.999	2.085
	Sensor placement	P1	A1	0.999	2.417
		P2	A2	0.999	2.800
		P3	A3	0.999	4.847
		P4	A1, A2	0.999	1.671
		P5	A1, A3	0.999	2.599
		P6	A2, A3	0.999	1.813
	Spring type	T1	Hardening	0.999	0.656
		T2	Anisotropic	0.999	0.369
Case III	Vertical spring			0.999	0.152
	Rotational spring			0.999	1.066

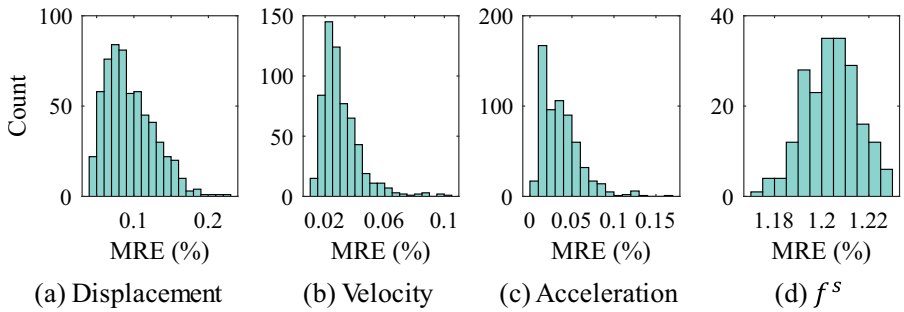

Fig. 7 MRE histogram of different responses in N0

Intel Core i7-13,700 CPU, 64 GB RAM, and an NVIDIA 4070 12 GB graphics card. The training time is 7.4 s for each epoch in this case.

The entire training process consisted of 1,000 epochs is illustrated in Fig. 5. Initially, the training and validation losses decrease sharply. After around 400 epochs, they exhibit significant oscillations. The training and validation loss curves closely align, suggesting no overfitting or underfitting phenomena during the training process.

The trained MLP with the smallest validation loss is selected as the final surrogate model. The learned and real boundary conditions are presented in Fig. 6. When the real displacement is in the range of the training displacement, the predicted nonlinearity is close to the ground truth. Table 2 presents R and MRE between the predicted and ground truth boundary conditions, with the displacement range for the indicator calculation defined as -0.1 m to 0.1 m.

Table 3 R and MRE values of different responses in all cases

Scenario	Response	R	MRE (%)
N0	Displacement	0.999	0.0946
	Velocity	0.999	0.0306
	Acceleration	0.999	0.0366
	Restoring force	0.999	1.204
Case II	Displacement	0.998	1.034
	Velocity	0.999	0.690
	Acceleration	0.999	0.772
	Restoring force	0.997	3.233
Case III	Displacement	0.999	0.0732
	Velocity	0.999	0.0585
	Acceleration	0.999	0.257
	Restoring force	0.999	0.848

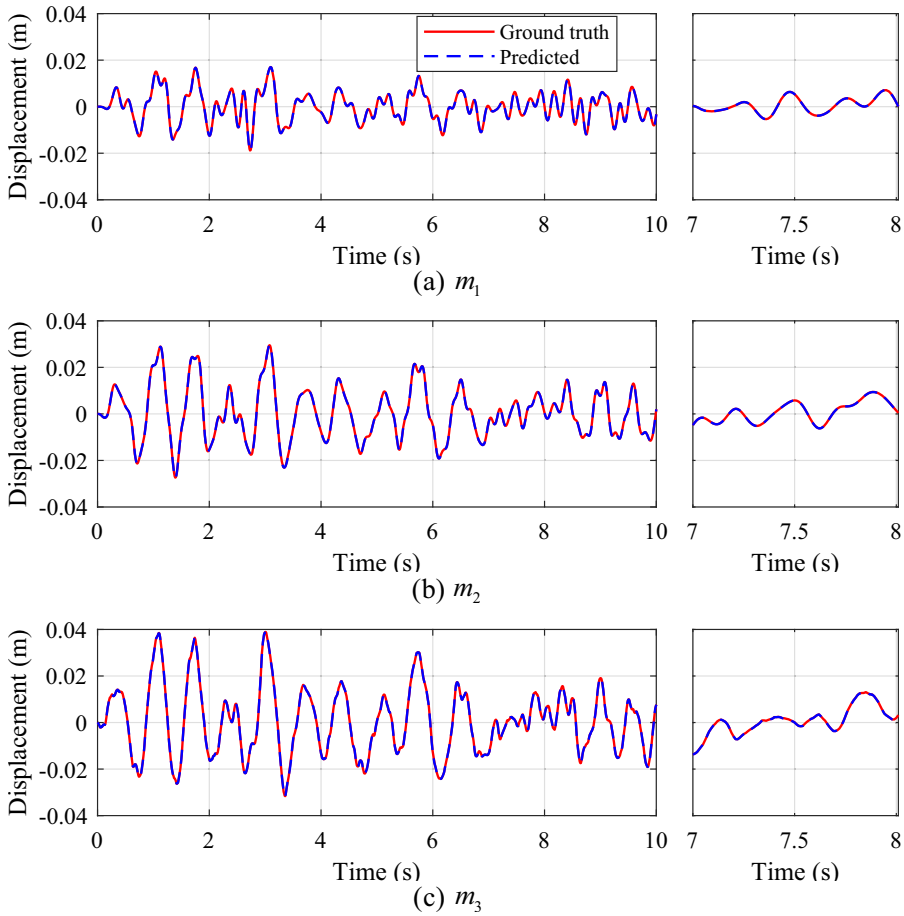

Fig. 8 Predicted and ground truth displacements of a new testing sample in N0

The result indicates R is very close to 1, and the MRE is 1.449%, indicating a high accuracy of the identified nonlinear boundary condition. However, when the measured displacement exceeds the training ranges, the MLP-predicted restoring force become less accurate. This phenomenon can be attributed to the inherent limitations of data-driven models, which are designed to learn only the behaviors represented within the training datasets. As a result, when test data exceeds this training range, the MLP's predictions may lack accuracy and reliability.

To verify the performance of the trained MLP in predicting structural dynamic responses, the histograms of MREs between predicted and measured structural responses in the validation sets, including the displacement, velocity, and acceleration of all masses and the restoring force of the nonlinear spring, are shown in Fig. 7. All the MREs are smaller than 5%. Moreover, the averaged R and MRE listed in Table 3 are close to 1 and smaller than 5%, respectively. These results indicate that the reconstructed responses are very accurate because the nonlinear boundary condition is well learned by the MLP.

The trained MLP model is also used to generate the full-field structural responses of a new testing sample that was not included in training. The testing sample lasts for 10 s. The predicted and ground truth displacements of all three masses are illustrated in Fig. 8, where they closely align with each other in overall shape and peak values. The results indicate a high generalization ability of the trained MLP.

4.2 Applicability discussion

4.2.1 Influence of measurement noise

Measurement noise is inevitable in practice, and it can lead to the overfitting effect. Therefore, the robustness

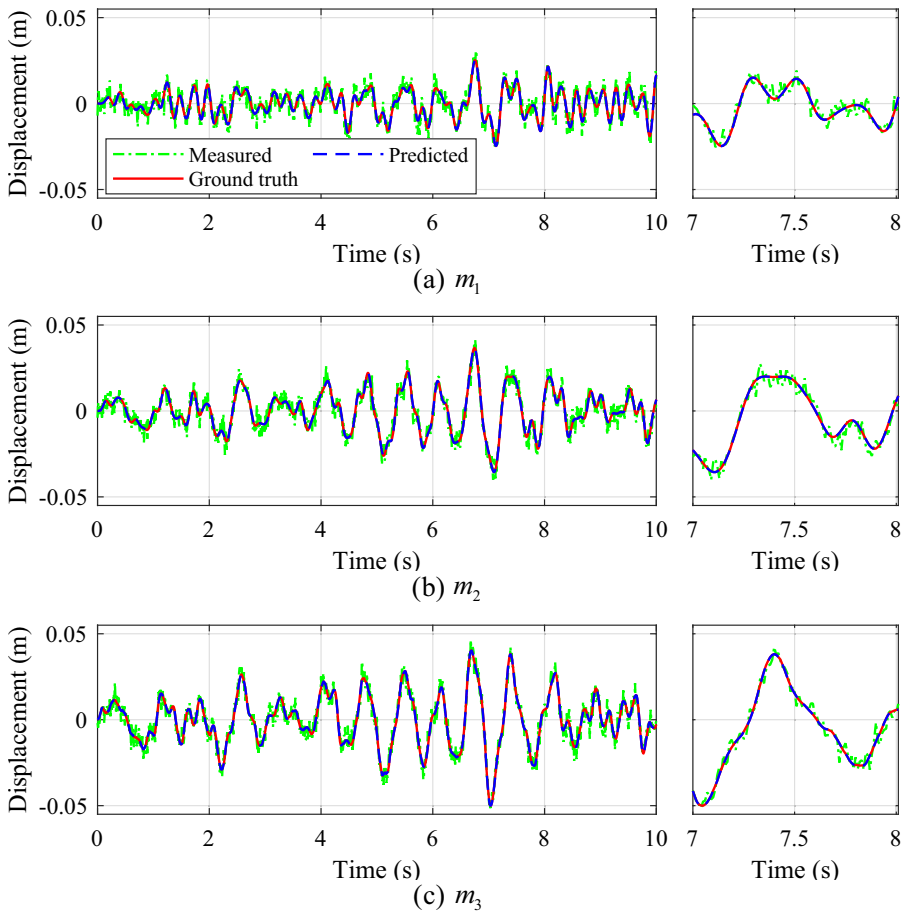

Fig. 9 Predicted and ground truth displacements of a new testing sample in N5

of the proposed method is further studied by using noisy measurements for training. The measured data are contaminated by the zero-mean Gaussian noise. The noised measurement is simulated as follows:

$$\tilde{\boldsymbol{R}} = \breve{\boldsymbol{R}} + NR * N\left(0, \frac{I}{N_s}\sum_{s=1}^{N_s} \mathrm{var}\left(\breve{\boldsymbol{R}}_s\right)\right) \tag{5}$$

where $\tilde{\boldsymbol{R}}$ represents the noised measurements,$\breve{\boldsymbol{R}}$ is the ground truth responses without noise, NR is the noise ratio, s denotes the sensor index, and N_s represents the total number of measurements of the same type. Four noise levels of 5%, 10%, 20%, and 30% are studied. The training settings are consistent with those in Sect. 4.1.

The calculated R and MRE at different noise levels are presented in Table 2. All R are close to 1, and MREs are less than 5%, indicating that the predicted boundary conditions are accurate in shape and time history. With the increase of noise, the MRE also increases but remains within 5%, and the highest MRE is 2.085%, suggesting that the influence of Gaussian noise is acceptable. These results all indicate that the proposed method exhibits strong robustness to noise.

The nonlinear boundary condition identified from the 30% noise-contaminated dataset is used to predict responses in a new testing set. Figure 9 shows the predicted, measured, and real displacements. The predicted response time history aligns with the ground truth, although the noise of the measurements is significant. This suggests that the nonlinear boundary condition identified with noised measurements is sufficiently accurate to predict the real responses.

4.2.2 *Influence of sensor placement*

In this subsection, different accelerator arrangements are used to investigate the influence of sensor placements. All possible sensor placement schemes for the

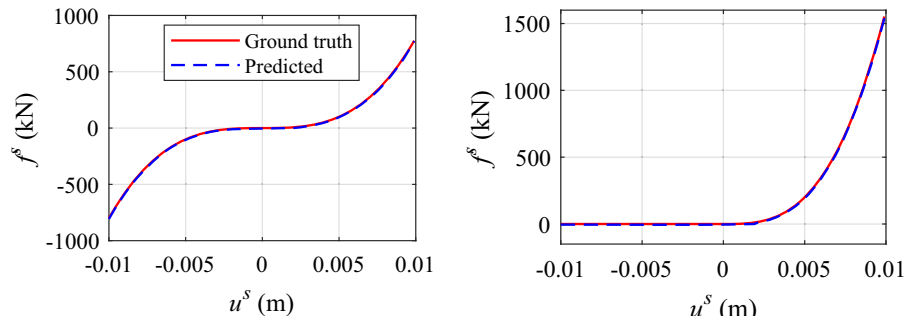

Fig. 10 Predicted boundary conditions of the hardening and anisotropic springs in T1 and T2

three-DOF spring-mass system are considered (Table 2). In this part, the noise ratio NR is set as 5%.

The comparison of indicators R and MRE is presented in Table 2. For all sensor placement schemes, R are close to 1, and the MRE is consistently less than 5%, indicating a high accuracy of the learned nonlinear models. Notably, the nonlinear boundary condition can be accurately identified even using A1 or A2. The calculated MRE decreases with the increase in sensor number. This suggests that the MLP can better learn the boundary condition with more optimization targets (sensor-measured data) being satisfied. Additionally, given only one accelerometer, the estimation MRE is the lowest when the sensor is installed at m_1. This is because the nonlinear spring is installed between the ground and m_1, and the response measured from A1 can provide more information about the nonlinearity model. The sensors should therefore be placed near the nonlinear component of the structure when arranging the sensor configuration.

4.2.3 Influence of boundary condition type

Two more types of nonlinear springs are investigated in this section: the hardening and anisotropic springs. Their restoring force-response curves are shown in Figs. 4b and c. The elastic hardening boundary is simulated by using a duffing spring that can describe the force–displacement relationships of disc springs [67] and the elastic suspension spring pair [68] in vibration isolation systems. The elastic orthotropic boundary condition is used to model tension-only (cable connections in cable-restrained high-damping rubber bearings [69]) and compression-only (elastic foundations [11]) boundary conditions.

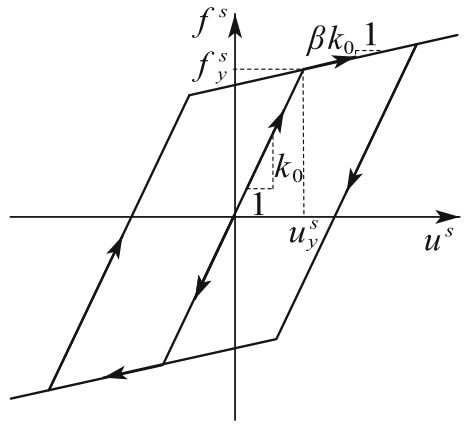

Fig. 11 Hysteretic curve of the bilinear model

The identified boundary conditions are presented in Fig. 10a and b. The identified models are consistent with their ground truth. The assessment indicators are reported in Table 2. R are all close to 1, and MREs are all smaller than 5%. The MRE of the anisotropic model is the smallest because the left part of the boundary condition is zero, similar to the initial state of the MLP where the weight and bias are all set as zeros, which will be seen again in Case III. Consequently, the training difficulty would decrease sharply in the anisotropic spring case, leading to a more accurate identified result.

5 Case II: A three-DOF spring-mass system with a hysteretic spring

The hysteretic boundary condition is further investigated in this section. The same three-DOF mass-spring system in Case I is used again. Here, the elastic spring connecting m_1 and the ground is replaced by a bilinear

hysteretic spring. The hysteretic curve is depicted in Fig. 11. The bilinear hysteretic model [70, 71] is defined by three parameters: initial stiffness k_0, yielding displacement u_y, and stiffness reduction factor β. In this case, k_0 is 4×10^5 kN/m, u_y is 5 mm, and β is 0.1. The initial stiffness is adopted when unloading. The bilinear boundary condition is commonly used to describe the hysteretic behaviors of lead rubber bearings, and laminated rubber bearings in earthquake engineering [4].

The MLP architecture exhibited in Fig. 2c is utilized to identify the hysteretic boundary condition. The MLP input should include the historical restoring force and displacement because the hysteretic model is path-dependent. The restoring force of a bilinear model theoretically relates merely to the restoring force, velocity, and displacement at the previous time step, and the hyperparameter k should therefore be 1. However, such prior knowledge is unknown when learning the nonlinear model, and k should therefore be set as a relatively large number. In Case II, k is taken as 2 and n is taken as 4, which includes the restoring force from the previous step and the displacements from the last three steps, to yield satisfactory results. The remaining hyperparameters for training are identical to those in Case I, as listed in Table 1.

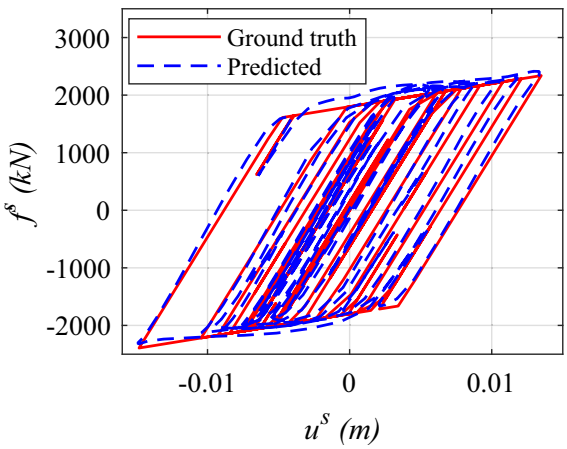

Fig. 12 Predicted and ground truth hysteretic curve of a new testing sample in Case II

The predicted and real hysteretic curves are displayed in Fig. 12 for a new testing set. The predicted hysteretic curve exhibits the same variational pattern, including loading, yielding, and unloading behaviors, as the ground truth. This indicates that the MLP has well learned the relationship between the loading history and the restoring force through its powerful nonlinear modeling capability. The observed discrepancy at sharp corners in the hysteretic curve arise because the MLP simulates the derivative $\frac{\partial MLP(\boldsymbol{x})}{\partial \boldsymbol{u}_i}$ through the backpropagation algorithm, as introduced in Sect. 2.2, which yields only finite derivatives. However, the derivative of the restoring force to displacement in the bilinear model at sharp corners is theoretically infinite. Consequently, it is challenging for the MLP to accurately fit the sharp turning points. The applicability of the MLP to the non-smooth nonlinearities can be improved by adding the training dataset, reducing the training noise level, increasing the network depth, and adjusting the activation functions, which may cause a higher computational burden.

The MREs of different types of response time history in the validation set are displayed in Fig. 13. Nearly all MREs are smaller than 5%, indicating the errors of reconstructed responses and restoring forces are acceptable. The means of R and MRE in the validation set are also reported in Table 3, suggesting that the predicted responses are accurate.

The trained MLP, representing the hysteretic boundary condition, is then used to predict structural responses. The predicted displacement time histories

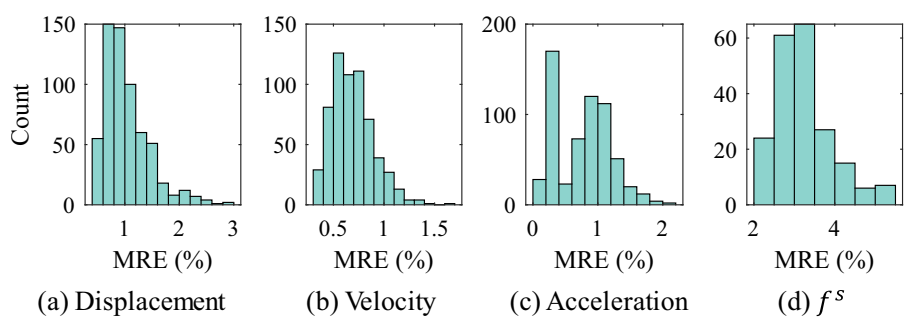

Fig. 13 MRE histogram of different responses in Case II

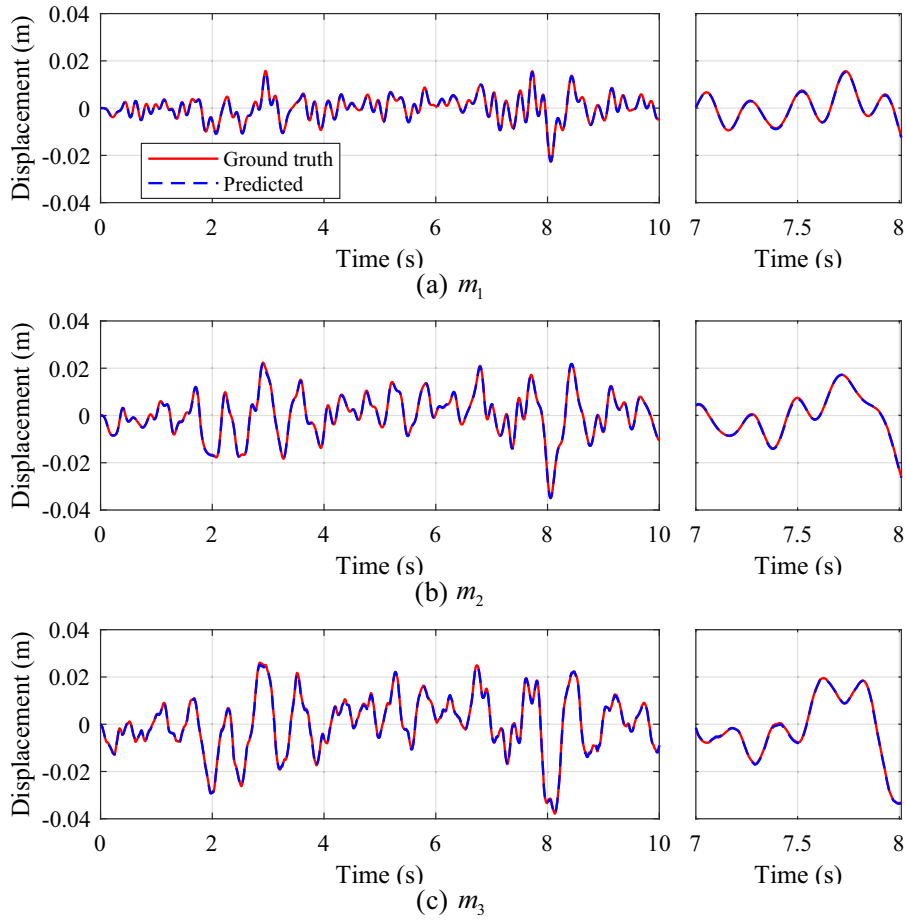

Fig. 14 Reconstructive displacement of three masses of a new testing sample in Case II

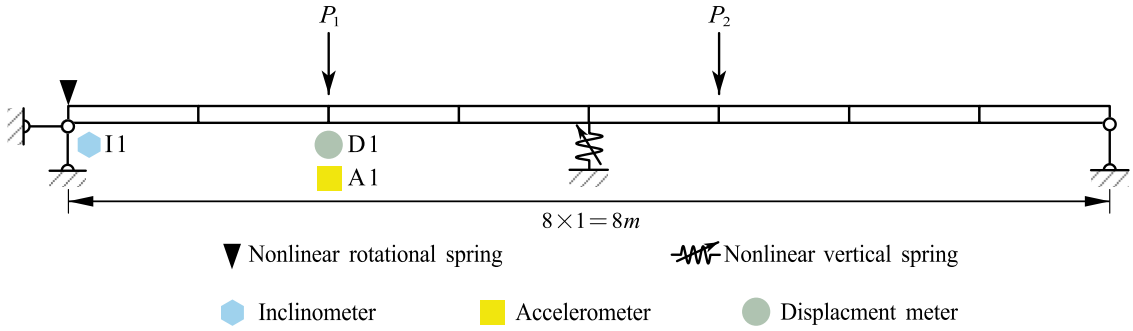

Fig. 15 Schematic of the beam model in Case III

of the testing set are displayed in Fig. 14, which fit well with the measured ones. This indicates that the hybrid model, combining the FE model and the well-trained MLP, can accurately simulate the responses of the considered hysteretic system.

6 Case III: A beam model with multiple elastic nonlinear springs

A beam model is used to verify the proposed method with nonlinearity at multiple positions, as shown in Fig. 15. The beam is divided into eight elements with only the in-plane deformation being considered,

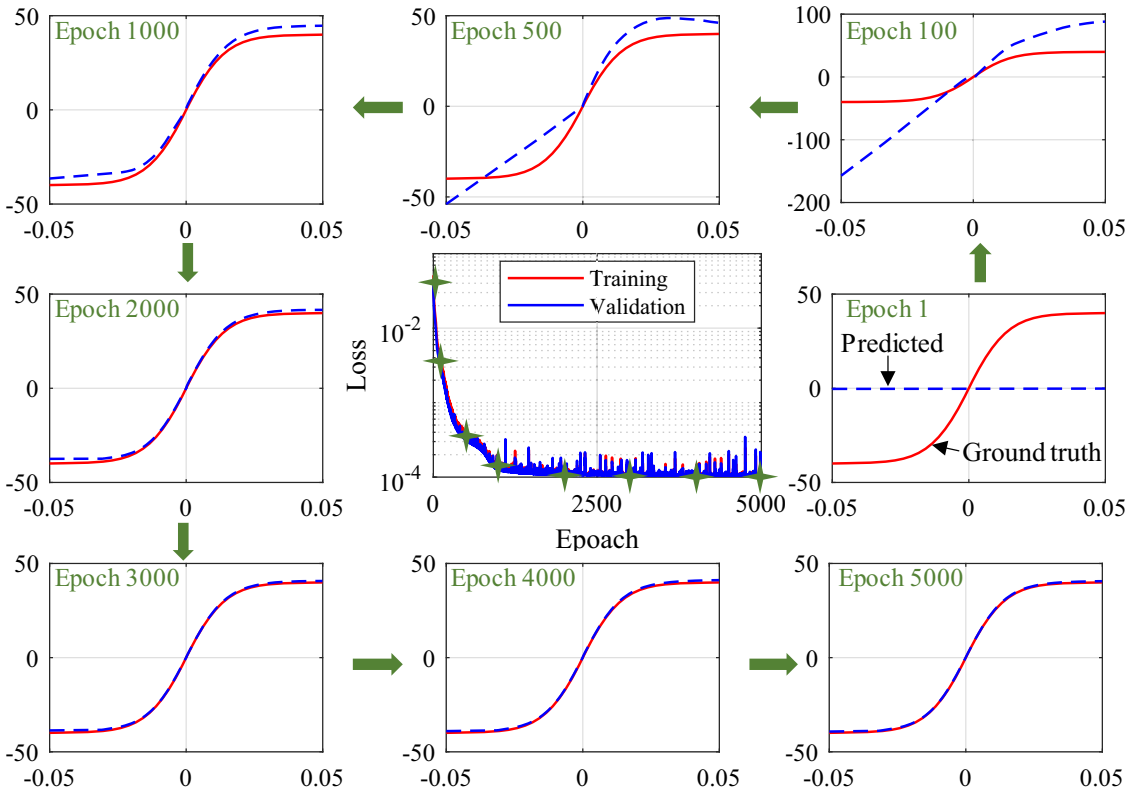

Fig. 16 Evolution process of the MLP representing the rotational nonlinear spring in Case III

resulting in 16 DOFs. The bending stiffness is 1.477×10^4 kN m^2, and the mass per unit length is 1.178×10^3 kg/m. The first two natural frequencies of the beam model are 2.748 and 10.997 Hz, and the associated damping ratios are both 2%. Subsequently, the linear damping matrix can be established. An elastic rotational softening nonlinear spring is connected to the left beam end, and a vertical hardening nonlinear spring is placed at the beam center. The maximum frequency ω_i^m with zero displacement is 5621.415 rad/s, and it is reduced by 24.252% when the selective mass scaling technique is applied. The white noise loads are applied to the nodes on the two spans. The accelerometers, tilters, and displacement transducers are used to measure structural responses at a sampling frequency of 1000 Hz.

The FEM-NN hybrid model is constructed using the mass, damping, and linear stiffness matrices and two MLPs associated with the two nonlinear springs. The model was trained by 5,000 epochs, and the other training settings are consistent with those in Case I. The loss curve and the corresponding evolution process of the MLP representing the rotational nonlinear spring are displayed in Fig. 16. Initially, the learned nonlinear model is a straight line with a constant value of zero, because the initial weights and biases of the MLP are set as 0. Then, the training and validating losses sharply drop, and after about 500 epochs, they oscillate below 3×10^{-4}. At around the 1,000th epoch, the learned boundary condition curve exhibits a similar shape to the ground truth but still has deviations. After 1,000 training epochs, the reduction of the training and validation losses is insignificant, whereas the predicted boundary condition curve continues to converge towards its ground truth. At this stage, the loss function, which represents the disparity between the reconstructed and measured responses, is primarily related with measurement noise and thus cannot be further reduced. However, the MLP is still making efforts to identify the true boundary condition with the noised data. Finally, after 5,000 epochs, the learned boundary conditions approach the true boundary conditions, as shown in the right-bottom subfigure in Fig. 16.

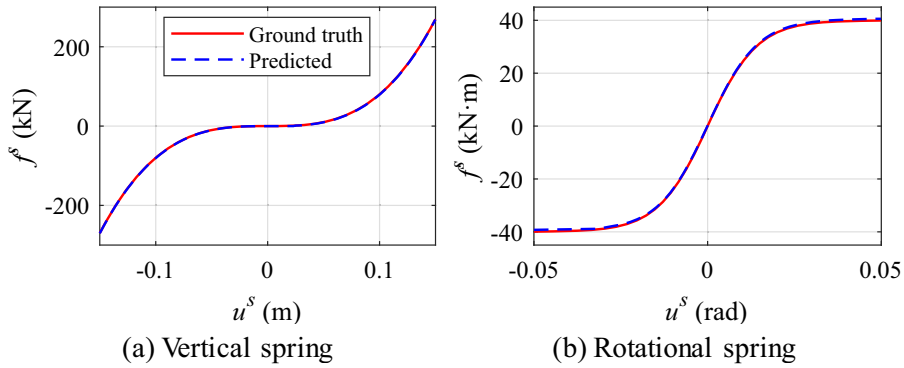

Fig. 17 Predicted boundary condition models of two nonlinear springs in Case III

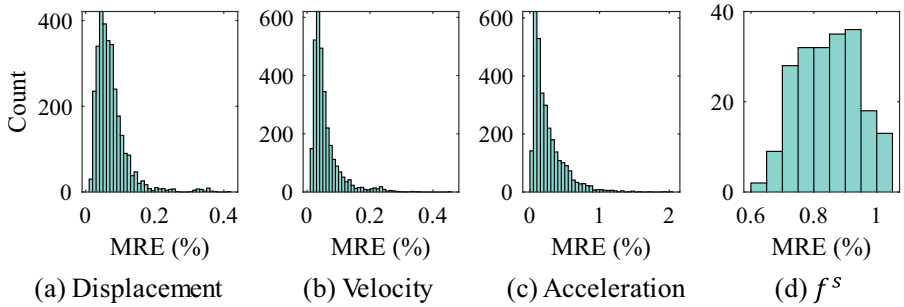

Fig. 18 MRE histogram of different responses in Case III

In the training process, the MLP learns the middle section (close to the origin of the horizontal coordinate) of the boundary condition more rapidly than other sections. This is because the structural responses to white noise excitation are normally distributed. As a result, the middle section in a boundary condition curve, which is close to zero, is more easily trained, benefiting from the concentration of training data. Correspondingly, the remaining sections of the boundary condition model are learned more slowly. Compared with Cases I and II, Case III requires more training iterations, indicating that with more DOFs and nonlinear models involved, the nonlinearity identification process would become challenging and time-consuming.

The learned boundary condition models are displayed in Fig. 17, and the evaluation indicators are reported in Table 2, where R is close to 1 and MREs are smaller than 1.5%. The results demonstrate that the accuracy of the identified nonlinear springs is satisfactory, and this approach can identify multiple nonlinear models simultaneously.

The MREs of the estimated response time histories in the validation dataset are exhibited in Fig. 18, and they are smaller than 1% in most cases. The mean values of the R and MRE are also presented in Table 3. These results collectively affirm the effectiveness of the hybrid model, incorporating the two well-trained MLPs, in accurately identifying the nonlinear structure and predicting its full-field responses.

7 Conclusions

An FEM-NN hybrid technique is developed to identify boundary conditions of the nonlinear system. The SCD solver is adopted and embedded to calculate structural nonlinear dynamic responses. The unknown nonlinear boundaries are surrogated by the MLPs, and the structural linear components are modeled by the FE method. The two components are assembled to formulate the global model. The proposed method is used to identify elastic, hysteretic, and multiple nonlinear boundaries of a three-DOF spring-mass system and a two-span continuous beam. The following conclusions can be drawn:

1) The developed hybrid model can accurately identify the elastic nonlinear boundary condition. The model is applicable to different noise conditions, sensor layouts, and nonlinear

boundary condition models. The hybrid model, incorporating the well-trained MLP, can also accurately predict full-field structural responses.

2) The bilinear hysteretic boundary condition model is correctly identified. In addition, the loading, yielding, and unloading behaviors are well modeled via the trained MLP model. By contrast, the sharply changing/turning points in a boundary condition model cannot be accurately identified by an MLP due to its nature as a continuous and differentiable function.
3) Multiple nonlinearities are correctly identified in the two-span continuous beam Case III. However, more iterations are required to achieve satisfactory results compared with Cases I and II because more nonlinear boundaries are included in Case III.

Author contributions Lanxin LUO: conceptualization, methodology, formal analysis, writing the original draft. Limin SUN: funding acquisition, supervision. Yixian LI: investigation, methodology, review & editing. Yong XIA: funding acquisition, review & editing, supervision.

Funding Open access funding provided by The Hong Kong Polytechnic University. This paper is supported by the National Natural Science Foundation of China (52378187) and the Technology Cooperation Project of Shanghai Qizhi Institute (SYXF0120020109).

Data availability No datasets were generated or analysed during the current study.

Declarations

Competing interest The authors declare no competing interests.

References

1. Kerschen, G., Worden, K., Vakakis, A.F., Golinval, J.-C.: Past, present and future of nonlinear system identification in structural dynamics. Mech. Syst. Signal Process. **20**, 505–592 (2006)
2. Noël, J.P., Kerschen, G.: Nonlinear system identification in structural dynamics: 10 more years of progress. Mech. Syst. Signal Process. **83**, 2–35 (2017)
3. Astroza, R., Ebrahimian, H., Conte, J.P.: Material parameter identification in distributed plasticity fe models of frame-type structures using nonlinear stochastic filtering. J. Eng. Mech. **141**, 04014149 (2015)
4. Zordan, T., Liu, T., Briseghella, B., Zhang, Q.: Improved equivalent viscous damping model for base-isolated structures with lead rubber bearings. Eng. Struct. **75**, 340–352 (2014)
5. Fang, C., Li, Y., Xu, Y.-L.: Nonlinear dynamic response of sea-crossing bridges to 3D correlated wind and wave loads. Adv. Struct. Eng. **25**, 3268–3283 (2022)
6. Gu, H.S., Itoh, Y.: Ageing behaviour of natural rubber and high damping rubber materials used in bridge rubber bearings. Adv. Struct. Eng. **13**, 1105–1113 (2010)
7. Teng, J., Tang, D.-H., Hu, W.-H., Lu, W., Feng, Z.-W., Ao, C.-F., et al.: Mechanism of the effect of temperature on frequency based on long-term monitoring of an arch bridge. Struct. Health Monit. **20**, 1716–1737 (2021)
8. Filipov, E.T., Fahnestock, L.A., Steelman, J.S., Hajjar, J.F., LaFave, J.M., Foutch, D.A.: Evaluation of quasi-isolated seismic bridge behavior using nonlinear bearing models. Eng. Struct. **49**, 168–181 (2013)
9. Chen, L., Sun, L., Nagarajaiah, S.: Cable with discrete negative stiffness device and viscous damper: passive realization and general characteristics. Smart Struct. Syst. **15**, 627–643 (2015)
10. Lu, Z., Wang, Z., Zhou, Y., Lu, X.: Nonlinear dissipative devices in structural vibration control: a review. J. Sound Vib. **423**, 18–49 (2018)
11. Pellicano, F., Mastroddi, F.: Nonlinear dynamics of a beam on elastic foundation. Nonlinear Dyn. **14**, 335–355 (1997)
12. Peel, H., Luo, S., Cohn, A.G., Fuentes, R.: Localisation of a mobile robot for bridge bearing inspection. Automat. Constr. **94**, 244–256 (2018)
13. Hoshiya, M., Saito, E.: Structural identification by extended Kalman filter. J. Eng. Mech. **110**, 1757–1770 (1984)
14. Wan EA, Merwe RVD. The unscented Kalman filter for nonlinear estimation. Proceedings of the IEEE 2000 Adaptive Systems for Signal Processing, Communications, and Control Symposium (Cat No00EX373)2000. p. 153–8.
15. Arasaratnam, I., Haykin, S.: Cubature kalman filters. IEEE Trans. Autom. Control **54**, 1254–1269 (2009)
16. Astroza, R., Ebrahimian, H., Conte, J.P.: Performance comparison of Kalman−based filters for nonlinear structural finite element model updating. J. Sound Vib. **438**, 520–542 (2019)
17. Huang, J., Lei, Y., Li, X.: An adaptive generalized extended Kalman filter for real-time identification of structural systems, state and input based on sparse measurement. Nonlinear Dyn. **112**, 5453–5476 (2024)

18. Wang, S., Lei, Y.: An unscented Kalman filter under unknown input without direct feedthrough for joint input and system identification of structural systems. Mech. Syst. Signal Process. **208**, 110951 (2024). https://doi.org/10.1016/j.ymssp.2023.110951
19. Lei, Y., Xia, D., Erazo, K., Nagarajaiah, S.: A novel unscented Kalman filter for recursive state-input-system identification of nonlinear systems. Mech. Syst. Signal Process. **127**, 120–135 (2019)
20. Tian, W., Weng, S., Xia, Y.: Model updating of nonlinear structures using substructuring method. J. Sound Vib. **521**, 116719 (2022)
21. Tian, W., Weng, S., Xia, Y.: Kron's substructuring method to the calculation of structural responses and response sensitivities of nonlinear systems. J. Sound Vib. **502**, 116101 (2021)
22. Song, M., Renson, L., Noël, J.-P., Moaveni, B., Kerschen, G.: Bayesian model updating of nonlinear systems using nonlinear normal modes. Struct. Control. Health Monit. **25**, e2258 (2018)
23. Song, M., Renson, L., Moaveni, B., Kerschen, G.: Bayesian model updating and class selection of a wing-engine structure with nonlinear connections using nonlinear normal modes. Mech Syst Signal Pr. **165**, 108337 (2022)
24. Kumar, K., Bhaumik, S., Date, P.: Extended kalman filter using orthogonal polynomials. IEEE Access. **9**, 59675–59691 (2021)
25. Liu, X., Gasco, F., Goodsell, J., Yu, W.: Initial failure strength prediction of woven composites using a new yarn failure criterion constructed by deep learning. Compos. Struct. **230**, 111505 (2019)
26. Sun, L., Shang, Z., Xia, Y., Bhowmick, S., Nagarajaiah, S.: Review of bridge structural health monitoring aided by big data and artificial intelligence: from condition assessment to damage detection. J. Struct. Eng. **146**, 04020073 (2020)
27. Wu, R.-T., Jahanshahi, M.R.: Deep convolutional neural network for structural dynamic response estimation and system identification. J. Eng. Mech. **145**, 04018125 (2019)
28. Zhang, R., Chen, Z., Chen, S., Zheng, J., Büyüköztürk, O., Sun, H.: Deep long short-term memory networks for nonlinear structural seismic response prediction. Comput. Struct. **220**, 55–68 (2019)
29. Li, Y., Ni, P., Sun, L., Xia, Y.: Finite element model-informed deep learning for equivalent force estimation and full-field response calculation. Mech Syst Signal Pr. **206**, 110892 (2024)
30. Chen, Z., Liu, Y., Sun, H.: Physics-informed learning of governing equations from scarce data. Nat. Commun. **12**, 6136 (2021)
31. Ni, P., Li, Y.X., Sun, L.M., Wang, A.: Traffic-induced bridge displacement reconstruction using a physics-informed convolutional neural network. Comput. Struct. **271**, 13 (2022)
32. Zhang, R., Liu, Y., Sun, H.: Physics-guided convolutional neural network (PhyCNN) for data-driven seismic response modeling. Eng. Struct. **215**, 110704 (2020)
33. Zhang, R., Liu, Y., Sun, H.: Physics-informed multi-LSTM networks for metamodeling of nonlinear structures. Comput. Methods Appl. Mech. Eng. **369**, 113226 (2020)
34. Liu, T., Meidani, H.: Physics-informed neural networks for system identification of structural systems with a multiphysics damping model. J. Eng. Mech. **149**, 04023079 (2023)
35. Zhai, W., Tao, D., Bao, Y.: Parameter estimation and modeling of nonlinear dynamical systems based on Runge-Kutta physics-informed neural network. Nonlinear Dyn. **111**, 21117–21130 (2023)
36. Yamaguchi, T., Mizutani, T.: A physics-informed neural network for the nonlinear damage identification in a reinforced concrete bridge pier using seismic responses. Struct. Control. Health Monit. **2024**, 5532909 (2024)
37. Sadeghi Eshkevari, S., Takáč, M., Pakzad, S.N., Jahani, M.: DynNet: physics-based neural architecture design for nonlinear structural response modeling and prediction. Eng. Struct. **229**, 111582 (2021)
38. Bacsa, K., Lai, Z., Liu, W., Todd, M., Chatzi, E.: Symplectic encoders for physics-constrained variational dynamics inference. Sci Rep-Uk. **13**, 2643 (2023)
39. Liu, W., Lai, Z., Bacsa, K., Chatzi, E.: Physics-guided deep markov models for learning nonlinear dynamical systems with uncertainty. Mech Syst Signal Pr. **178**, 109276 (2022)
40. Liu, W., Lai, Z., Bacsa, K., Chatzi, E.: Neural extended Kalman filters for learning and predicting dynamics of structural systems. Struct. Health Monit. **23**, 1037–1052 (2024)
41. Liu, X., Tian, S., Tao, F., Yu, W.: A review of artificial neural networks in the constitutive modeling of composite materials. Compos. B Eng. **224**, 109152 (2021)
42. Wang, X., Yin, Z.Y., Wu, W., & Zhu, H.H.: Neural network-augmented differentiable finite element method for boundary value problems. Int. J. Mech. Sci. 109783 (2024)
43. Wang, X., Yin., Z.Y.: Interpretable physics-encoded finite element network to handle concentration features and multi-material heterogeneity in hyperelasticity. Comput. Methods Appl. Mech. Eng. **431**, 117268 (2024)
44. Ghaboussi, J., Sidarta, D.E.: New nested adaptive neural networks (NANN) for constitutive modeling. Comput. Geotech. **22**, 29–52 (1998)
45. Ghaboussi, J., Pecknold, D.A., Zhang, M., Haj-Ali, R.M.: Autoprogressive training of neural network constitutive models. Int. J. Numer. Meth. Eng. **42**, 105–126 (1998)
46. Yun, G.J., Ghaboussi, J., Elnashai, A.S.: Self-learning simulation method for inverse nonlinear modeling of cyclic behavior of connections. Comput. Methods Appl. Mech. Eng. **197**, 2836–2857 (2008)
47. Huang, D.Z., Xu, K., Farhat, C., Darve, E.: Learning constitutive relations from indirect observations using deep neural networks. J. Comput. Phys. **416**, 109491 (2020)
48. Liu, X., Tao, F., Haodong, D., Wenbin, Y., Kailai, X.: Learning nonlinear constitutive laws using neural network models based on indirectly measurable data. J. Appl. Mech. (2020). https://doi.org/10.1115/1.4047036
49. Xu, K., Tartakovsky, A.M., Burghardt, J., Darve, E.: Learning viscoelasticity models from indirect data using deep neural networks. Comput. Methods Appl. Mech. Eng. **387**, 114124 (2021)
50. Clough RW, Penzien J. Dynamics of Structures: McGraw-Hill; 1993.
51. Butcher, J.C.: A history of Runge-Kutta methods. Appl. Numer. Math. **20**, 247–260 (1996)
52. Wu, B., Bao, H., Ou, J., Tian, S.: Stability and accuracy analysis of the central difference method for real-time

substructure testing. Earthq Eng Struct D. **34**, 705–718 (2005)
53. Soares, D., Großeholz, G.: Nonlinear structural dynamic analysis by a stabilized central difference method. Eng. Struct. **173**, 383–392 (2018)
54. Olovsson, L., Simonsson, K., Unosson, M.: Selective mass scaling for explicit finite element analyses. Int. J. Numer. Meth. Eng. **63**, 1436–1445 (2005)
55. Sze, V., Chen, Y.H., Yang, T.J., Emer, J.S.: Efficient processing of deep neural networks: a tutorial and survey. Proc. IEEE **105**, 2295–2329 (2017)
56. Jian, X., Xia, Y., Chatzi, E., Lai, Z.: Bridge influence surface identification using a deep multilayer perceptron and computer vision techniques. Struct. Health Monit. **23**, 1606–1626 (2023)
57. de Oliveira Dos Santos, J.P., Crémona, C., da Silveira, A.P.C., Oliveira de Martins, L.C.: Real-time damage detection based on pattern recognition. Str. Concrete **17**, 338 (2016)
58. Goswami, S., Bhattacharya, P.: A scalable neural-network modular-array architecture for real-time multi-parameter damage detection in plate structures using single sensor output. Int. J. Comput. Intell. Appl. **11**, 1250024 (2012)
59. Fallahian, M., Khoshnoudian, F., Meruane, V.: Ensemble classification method for structural damage assessment under varying temperature. Struct. Health Monit. **17**, 747–762 (2017)
60. Pei, J.-S., Smyth, A.W.: New approach to designing multilayer feedforward neural network architecture for modeling nonlinear restoring forces. I: formulation. J. Eng. Mech. **132**, 1290–1300 (2006)
61. Pei, J.-S., Mai, E.C., Wright, J.P., Masri, S.F.: Mapping some basic functions and operations to multilayer feedforward neural networks for modeling nonlinear dynamical systems and beyond. Nonlinear Dyn. **71**, 371–399 (2013)
62. Rosenblatt, F.: The perceptron: a probabilistic model for information storage and organization in the brain. Psychol. Rev. **65**, 386 (1958)
63. Goodfellow I. Deep learning: MIT press; 2016.
64. Paszke A, Gross S, Massa F, Lerer A, Bradbury J, Chanan G et al. Pytorch: An imperative style, high-performance deep learning library. Advances in neural information processing systems. 2019;32.
65. Rao, C., Sun, H., Liu, Y.: Physics-informed deep learning for computational elastodynamics without labeled data. J. Eng. Mech. **147**, 04021043 (2021)
66. Anastasio, D., Marchesiello, S., Svelto, C., Gatti, G.: Experimental characterization of a nonlinear mechanical oscillator with softening behaviour for large displacements. Nonlinear Dyn. **112**, 7817–7830 (2024)
67. Miyamoto, K., Iba, J., Watanabe, K., Ishii, K., Kikuchi, M.: Development of nonlinear geometric seismic isolation with a duffing spring. Struct. Control. Health Monit. **2023**, 3917013 (2023)
68. Ibrahim, R.A.: Recent advances in nonlinear passive vibration isolators. J. Sound Vib. **314**, 371–452 (2008)
69. Fang, C., Liang, D., Zheng, Y., Lu, S.: Seismic performance of bridges with novel SMA cable-restrained high damping rubber bearings against near-fault ground motions. Earthq Eng Struct D. **51**, 44–65 (2022)
70. Iwan WD. The dynamic response of bilinear hysteretic systems. 1961.
71. Katsaras, C.P., Panagiotakos, T.B., Kolias, B.: Restoring capability of bilinear hysteretic seismic isolation systems. Earthq Eng Struct D. **37**, 557–575 (2008)